Large-Scale Micro- and Nanopatterns of Cu(In,Ga)Se_2 Thin Film Solar Cells by Mold-Assisted Chemical-Etching Process

Yi-Chung Wang,[†,§] Hsiang-Ying Cheng,[†,§] Yu-Ting Yen,[†] Tsung-Ta Wu,[†,‡] Cheng-Hung Hsu,[†] Hung-Wei Tsai,[†] Chang-Hong Shen,[‡] Jia-Min Shieh,[‡] and Yu-Lun Chueh*[,†]

[†]Department of Materials Science and Engineering, National Tsing Hua University, Hsinchu 30013 Taiwan and [‡]National Nano Device Laboratories, No. 26, Prosperity Road 1, Hsinchu 30078, Taiwan. [§]Y.-C.W. and H.-Y.C. contributed equally to this work.

ABSTRACT A reactive mold-assisted chemical etching (MACE) process through an easy-to-make agarose stamp soaked in bromine methanol etchant to rapidly imprint larger area micro- and nanoarrays on CIGS substrates was demonstrated. Interestingly, by using the agarose stamp during the MACE process with and without additive containing oil and triton, CIGS microdome and microhole arrays can be formed on the CIGS substrate. Detailed formation mechanisms of microstructures and the chemical composition variation after the etching process were investigated. In addition, various microand nanostructures were also demonstrated by this universal approach. The microstructure arrays integrated into standard CIGS solar cells with thinner thickness can still achieve an efficiency of 11.22%, yielding an enhanced efficiency of ~18% compared with that of their planar counterpart due to an excellent absorption behavior confirmed by the simulation results, which opens up a promising way for the realization of high-efficiency micro- or nanostructured thin-film solar cells. Finally, the complete dissolution of agarose stamp into hot water demonstrates an environmentally friendly method by the mold-assisted chemical etching process through an easy-to-make agarose stamp.

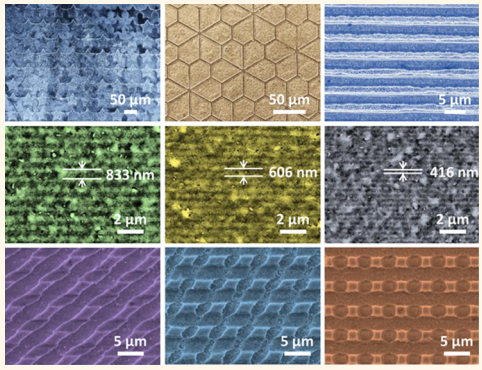

KEYWORDS: Cu(In · Ga)Se_2 · agarose stamp · microand nanostructures · mold-assisted chemical-etching process

Cu(In, Ga)Se_2 (CIGS) is one of the most promising absorber materials for thin-film solar cells due to its high optical absorption coefficient, tunable band gap, and good thermal stability.[1,2] The latest record efficiency of 21.7% further shows the unexplored technical potential of CIGS solar cells.[3] However, to compete with other photovoltaic technologies, one major hurdle is the cost of scarce raw materials such as indium (In) and selenium (Se), limiting the mass production.[4] To cut cost per watt, exploiting different technologies is of paramount importance for reducing the absorber thickness while keeping the high conversion efficiency. Researchers are now investigating efficient light-trapping schemes for the next-generation solar cells such as diffraction gratings,[5,6] photonic crystals,[7,8] and plasmonic nanostructures[9] to achieve the ultimate goal of maximizing solar energy received by the minimal volume of absorber. Among them, micro- or nanostructured absorber layers[10−12] without introduction of new materials are widely introduced to enhance the light harvesting by either multiple scattering or excitation of its local or guide resonances inside the designed structures. However, recent studies have revealed the serious Auger and surface recombination at the drastically increased surface and interface areas to volume ratios in the cases of nanostructured Si solar cells.[10] In addition to the junction area increment, the risks for damaging the surface and deteriorating the bulk quality have to be taken into account. For example, CIGS nanotip solar cells without proper post-treatment are prone to performance deterioration.[13] To achieve effective light

* Address correspondence to ylchueh@mx.nthu.edu.tw.

Received for review December 16, 2014 and accepted February 27, 2015.

Published online March 13, 2015
10.1021/acsnano.5b00701

management while leaving minimal increments in the junction area, the simplest light-trapping scheme based on diffractive microstructures shows fertile opportunity.[14−16]

For (110) single-crystalline silicon solar cells, simple alkaline or acidic wet etching process is commonly applied for surface texturing,[17,18] which is, however, not applicable to CIGS and the other thin-film absorbers. Several lithographic techniques such as photolithography and RIE do exist,[16,19] but many of them are either complex or expensive for mass production, and the etching process may induce surface damage to the absorbers. Therefore, micro- or nanoimprinting lithography becomes a cost-effective alternative large-scale roll-to-roll process to fabricate antireflection layers in PV industrials.[20,21] Nonetheless, large-area transfer of desired patterns onto hard or nondeformable substrates has stringent requirements for surface roughness for uniformity of mechanical deformation or curing of resist layers. In addition, fragile, expensive, and consumable master mold is easily damaged during the imprinting process due to the shear force or trapped particles. Normally, microcontact printing (μ-CP) uses soft and elastomeric molds, such as polydimethylsiloxane, which could eliminate the air gap between the mold and the substrate to enhance the conformity.[22,23] However, to create micro- or nanoengraved topographies into hard, rigid materials requires either a series of processes requiring masking or photoresistant layers which often cause peeling or underetching. Hence, developing alternative methods capable of implementing arbitrarily designed surface morphologies on CIGS solar cells without deterioration in film quality or device performance still poses a challenge.

In 2005, Grzybowski reported a maskless imprinting process using agarose stamps by a mold-assisted chemical etching (MACE) process.[24,25] Since the etchant or oxidant at the stamp/substrate interface is continuously replenished, the reaction can proceed for longer periods than that of μ-CP. The easy-to-make hydrogel stamps soaked into chemical etchant could successfully engrave micro- and nanopatterns into metals, glasses, or semiconductors with resolutions down to 300 nm. This technique involves fewer processing steps than NIL or μ-CP and circumvents solution spin-coating or curing processes, leading to advantages of the low-cost process and high repeatability with a large printing area. In this regard, we demonstrated a low cost MACE technique using patterned hydrogel stamps soaked in bromine methanol etchant to contact print arbitrarily designed surface morphologies onto CIGS substrates over large areas. We also established a new method to prepare either positive or negative patterns with the same contact printing stamp by simply controlling the spread of additive. The X-ray photoelectron spectroscopic (XPS) analysis confirmed that the compositions of the etched CIGS surface remained unchanged; therefore, our MACE technique does not require additional post-treatment. To realize the concept of light management in CIGS solar cells, we chose three-dimensional (3D) microhole arrays (MHAs) and microdome arrays (MDAs) to remove the polarization dependence and ensure structural simplicity. Furthermore, light trapping characteristics of MHAs and MDAs stamped on the surface of CIGS thin films were investigated carefully compared to that of their planar counterpart. Findings indicate that the CIGS MHAs and MDAs have the ability to locally diffract and guide incident light into longer optical paths compared with that of planar CIGS thin films with the same thickness and thus enhance the light absorption. For the first time, we demonstrate the CIGS-microstructured solar cell with the highest conversion efficiency reaching to 11.22% with the efficiency enhancement of ~18% compared with its planar counterpart. Finally, the complete dissolution of the agarose stamp into the hot water demonstrates an environmentally friendly method by the MACE process through an easy-to-make agarose stamp.

RESULTS AND DISCUSSION

Figure 1 illustrates the MACE process directly on CIGS substrates. A typical procedure starts with a Si master stamp with a target geometry prepared by photolithography and reactive ion etching processes (Figure 1a). The SEM images of the Si master stamp and the corresponding agarose stamp are shown in Figure S1 (Supporting Information). Replicas of micropatterned hydrogel were made from 8 wt % solution of agarose by hot casting against the Si master stamp at

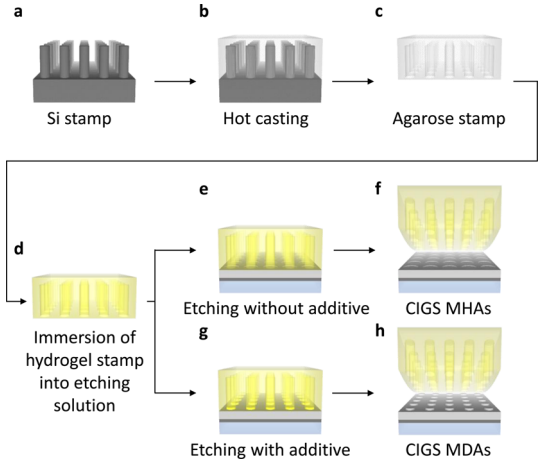

Figure 1. Process flows of replicating Si master stamp. (a) Si master stamp with microrod array replicated by (b) hot agarose gel casting; (c) whitish agarose stamp with micropore arrays was obtained after peeling it off the Si master stamp; (d) yellow agarose stamp was obtained after 2-h immersion in bromine/methanol solution; (e, f, g, h) process flow of the MACE process e without and g with additive to prepare f CIGS MHAs and h CIGS MDAs, respectively.

95 °C for 2 h (Figure 1b). After cooling and gelation processes, the whitish and flexible agarose layer was carefully peeled off and cut into 2 cm × 2 cm × 0.5 cm rectangular agarose stamps patterned with the negative feature arrays in the Si master stamp (Figure 1c). Note that the used Si master stamp can be cleaned and reused limitlessly. For the MACE process, the agarose stamp was soaked in 0.15 M bromine/methanol etchant for 2 h (Figure 1d). The etching process starts once the stamp touchs the CIGS substrate under a slight pressure of ~70 g/cm^2 to maintain a conformal contact. The whole process, in this configuration, is governed by two reaction-diffusion (RD) processes, including continuously refreshing the etchant to and removing the reactant from the CIGS/agarose interface, which enables agarose stamp to engrave the CIGS surface. Therefore, we could obtain the CIGS microstructure arrays replicating the surface morphology of the Si master with high fidelity. To prevent the capillary wetting of the etchant and the resulting lateral etching during the etching process, mineral oil is usually applied at the interface of the hydrogel stamp. In addition, surfactant is required for the uniform spreading of mineral oil. As a result, either positive microdome arrays (MDAs) or negative microhole arrays (MHAs) can be synthesized using the same agarose stamp after the MACE process with or without additives (mineral oil containing surfactant 0.1 V% Triton X-100) (Figure 1e−h).

Parts a−d of Figure 2 show the photographs, optical microscopy (OM), and scanning electron microscopy (SEM) images of CIGS MDAs and MHAs prepared by 20 min of the MACE process with the identical agarose stamp. The dark- and bright-field OM images clearly show that the MACE process can faithfully imprint both kinds of morphologies without distortion (Figure 2a,b). The insets in Figure 2a,b show photographs of the uniform contact printing of CIGS MDAs and MHAs over a 2 × 2 cm^2 area, depending on the original pattern area of Si master mold. The front sides of both CIGS substrates consist of grating microstructure arrays, enabling the CIGS thin films to scatter incident light into a distribution of angles. Both microstructures sharing same grating periodicity show drastic but similar color change observed by the naked eye. Dark-field optical microscope images further indicate the scattering of incident light occurred at the edge of the microstructures. From the SEM images (Figure 2c,d), the pattern height of CIGS MDAs is higher than that of CIGS MHAs. The etched surfaces of both kinds of microstructures are smooth, and no cracks or pits are observed as shown in the magnified SEM images in insets of Figure 2c,d. In addition, characterization of surface morphologies by atomic force microscopy (AFM) (Figure 2e,f) shows the average pattern heights of CIGS MDAs and MHAs are 854.7 and 184.5 nm, respectively. (See the Supporting Information for AFM images of pristine (Figure S2a) and CIGS without

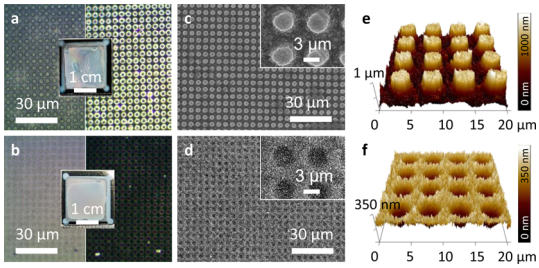

Figure 2. (a, b) Bright-field and dark-field optical microscopy images and photographs of CIGS MDAs and MHAs. (c, d) Scanning electron microscopy images of CIGS MDAs and MHAs. (e, f) Atomic force microscopy images of e, CIGS MDAs, and f, MHAs.

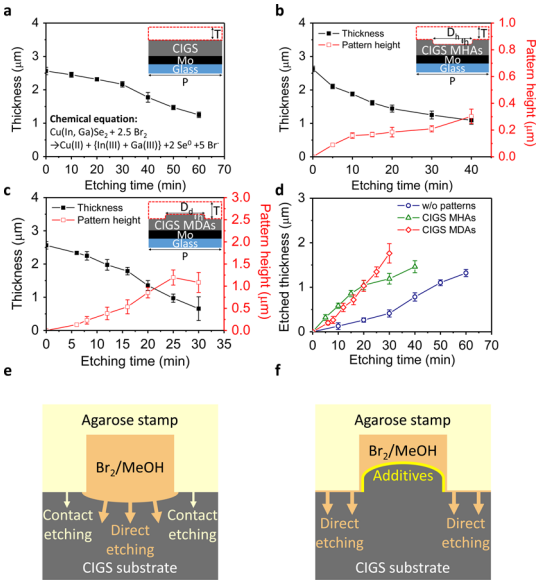

Figure 3. Thickness and pattern height difference of CIGS (a) without patterns, (b) CIGS MHAs, and (c) CIGS MDAs as functions MACE duration. (d) Etched thickness *versus* MACE duration. (e, f) Proposed microstructure formation mechanism of e, CIGS MHAs, and f, CIGS MDAs.

patterns (Figure S2b) and more surface parameters of all types of structures (Table S1).)

Furthermore, to shed light on etching mechanisms, etch rates between CIGS MDAs, MHAs, and flattened CIGS thin films (w/o patterns) are compared in Figure 3a−c. The thickness reduction rates of CIGS MDAs and MHAs are obviously higher than that of without patterns, but it would be more explicit to compare the effective etched thickness according to the simplified configurations shown in the insets in Figure 3a−c of the CIGS thin films without patterns, CIGS MDAs, and CIGS MHAs, respectively. The geometric parameters for etched thickness calculation are listed in Table 1. Note that the diameters of CIGS MHAs are usually larger than those of MDAs due to the lateral etching. Figure 3d shows the calculated etched CIGS thickness as a function of etching time without patterns, CIGS MDAs, and CIGS MHAs. The etch rates of CIGS MDAs and CIGS MHAs were comparable to each other at the initial

TABLE 1. Structural Parameters for Etch Rate Calculation

	without pattens	MDAs	MHAs
etched thickness	T	$T - (\pi/4)(D_d/P)^2h$	$T + (\pi/4)(D_h/P)^2h$
etch rate (nm/s)	0.338	0.907	0.914

D_d = 2500 nm, D_h = 4000 nm, P = 5000 nm.

stage of the MACE process; however, the etch rate by flattening is significantly slow, suggesting that microstructures on stamps significantly affect the etching rate.

To elucidate the proposed mechanism of microstructure formation, we performed the curve fitting of the volume etch rate according to the one-dimensional (1-D) RD equation.[26] We assume that (1) the reaction products are continuously removed from the MACE interface, the (2) diffusion rate of the etchant is significantly faster than the interface reaction rate ($\alpha^2 t/D \gg 1$), and (3) the initial condition of $c(x, t = 0) = c_0$ at the boundary condition of $c(x = \infty, t) = c_0$ with $D(\partial c \partial x) = \partial c(x = 0, t)$. The etch rate becomes time-independent from ($dT/dt = \alpha c_0 V_{CIGS}$) where α is the proportional constant and V_{CIGS} is the molar volume of CIGS, which agrees well with the case of CIGS without patterns, CIGS MDAs, and CIGS MHAs within the first 20 min where the etching rates (nm/s) of 0.338, 0.907, and 0.914 can be calculated, respectively. The etch rate deviation of CIGS MHAs most likely resulted from the evaporation of residual etchant because of incomplete seal during the MACE process. The significantly slow etch rate by flattening is because the average concentration of bromine–methanol etchant inside the agarose matrix is lower than that inside the micropore arrays (MPAs) of agarose stamp. The etching models of CIGS MHAs and MDAs were proposed as shown in Figure 3e,f in terms of contact and direct etching by the etchant inside the agarose matrix or the MPAs of the agarose stamp, respectively. After removal of the agarose stamps from the etching solution, the bromine–methanol etchant can exist inside the MPAs and the agarose matrix, leading to direct and contact etching once the agarose stamp makes contact with the CIGS substrate. Because the etch rate of direct etching is higher than that of contact etching, the etching proceeds faster under the MPAs of the agarose stamp rather than the contact area between the agarose stamp and the CIGS substrates, eventually resulting in the formation of MHAs (Figure 3e). However, if we spread the additives on the CIGS thin films before the MACE process, those direct etching by the residual etchant inside MPAs of agarose stamp would be retarded by additives, so the etching process can only take place within the contact area rather than under the MPAs of the agarose stamp, resulting in an opposite etching behavior and leading to the formation of CIGS MDAs (Figure 3f). Findings indicate that the

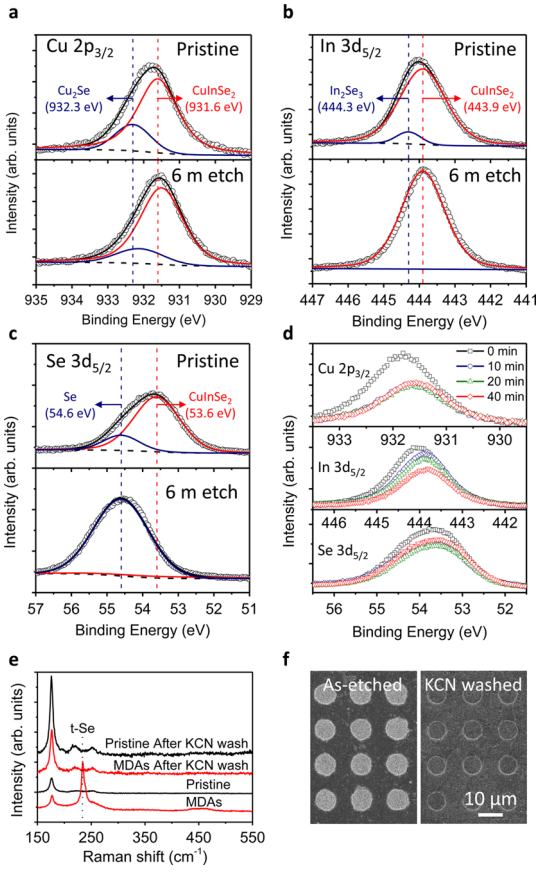

Figure 4. X-ray photoelectron spectra of (a) Cu $2p_{3/2}$, (b) In $3d_{5/2}$, and (c) Se $3d_{5/2}$ before and after 6 min etch. (d) X-ray photoelectron spectra of Cu $2p_{3/2}$, In $3d_{5/2}$, and Se $3d_{5/2}$ before and after 10, 20, and 40 min etch. (e) Raman spectra of pristine CIGS and CIGS MDAs before and after the KCN wash. (f) SEM images of CIGS MDAs before and after the 10 min KCN wash.

MACE process is able to provide two kinds of microstructures from a single patterned agarose stamp with or without addition of additives.

To shed light on the reaction mechanism from the MACE process, we investigated the surface chemical properties of CIGS thin film and MDAs with an etching time of 6 min by X-ray photoelectron spectroscopic (XPS) as shown in Figure 4a–c. Obvious peaks located at 932.3 and 444.3 eV deconvoluted from Cu $2p_{3/2}$ and In $3d_{5/2}$, corresponding to Cu_2Se[27] and In_2Se_3[28] phases, confirm the existence of secondary phases in the pristine CIGS film phases. In addition, residual amorphous Se (a-Se)[28] can be also found in the pristine CIGS film confirmed by the peaks at 55 eV deconvoluted from Se $3d_{5/2}$. In contrast, no obvious peak shift can be observed in Ga $2p_{3/2}$ after 6 min etch (Figure S3a, Supporting Information). Interestingly, after the MACE process at 6 min etch, the peaks at 932.3 and 444.3 eV for Cu $2p_{3/2}$ and In $3d_{5/2}$ can be significantly reduced, indicating the removal of Cu_2Se and In_2Se_3 secondary phases on the CIGS substrates. However, $CuInSe_2$[28] peak at 53.6 eV deconvoluted from Se $3d_{5/2}$ observably disappears, and the a-Se peak at 55 eV can be exactly

TABLE 2. XPS Analysis of Surface Composition

	[Cu] (atom %)	[In] (atom %)	[Ga] (atom %)	[Se] (atom %)
pristine	9.59	23.92	12.27	54.22
6 min etch	8.71	22.75	10.13	58.41

confirmed. The Se enrichment on the surface of CIGS substrate could be ascertained by the corresponding compositions of the pristine CIGS film, and the CIGS MDAs extracted from XPS results are shown in Table 2, which is also consistent with the report from the literature due to the preferential dissolution of the metals (Cu, In and Ga) aqueous bromine solution, leaving Se^0 on the surface by the chemical reaction of $Cu(In,Ga)Se_2 + 2.5Br_2 \rightarrow Cu(II) + \{In(III) + Ga(III)\} + 2Se^0 + 5Br^-$.[29] We further analyzed the surface chemical properties of the CIGS MDAs synthesized by the MACE process from 10 to 40 min. The peaks for $2p_{3/2}$, In $3d_{5/2}$, Se $3d_{5/2}$, and Ga $2p_{3/2}$ as shown in Figure 4d and Figure S3b (Supporting Information) remain unchanged during the MACE process from 10 to 40 min, indicating that the longer etching time does not alter the surface chemical properties of the CIGS MDAs. The peak of Se $3d_{5/2}$ at 53.6 eV suggests that the a-Se at the early stage would be dissolved after etching times longer than 10 min and surface properties would be the same as that of the pristine CIGS film. The results are similar to wet etching of CIGS thin films by aqueous bromine solution and can be explained by the oxidation of Se^0 by the bromine through the rate-determining step: $Se^0 + 2Br_2 \rightarrow Se(IV) + 4Br^-$. In addition, the Se-rich surface could be removed by potassium cyanide (KCN) wash treatment, leaving a surface of bulk CIGS.[30] Thus, we used KCN wash treatment to remove the Se-rich layer on CIGS MDAs, and the effect of KCN wash treatment was characterized by Raman spectroscopy as shown in Figure 4e. Obviously, a peak at 234 cm^{-1} appears, representing existence of the t-Se phase.[31] After the 10 min KCN wash treatment, the 234 cm^{-1} peak disappears and the spectrum is similar to that of the pristine CIGS thin film. Moreover, from the SEM images shown in Figure 4f, particles on the surface of CIGS MDAs, representing the excess Se on the Se-rich layer, could be completely removed after the 10 min KCN wash treatment. More evidence of the coexistence of the local Se signal examined by Raman spectra is shown in Figure S4 (Supporting Information). In summary, the Se-rich layer would form at early stage of MACE process and be dissolved again with longer etching time. Similarly, in the cases of applying additive, the residual etchant inside agarose stamp can barely etch the CIGS films under the MPAs of the agarose stamp, leading to the slightly etched surface of the CIGS MDAs covered by the Se-rich layer.

In addition to creating CIGS MDAs and MHAs, various types of microstructures, including two-dimensional (2D) microstar, follower, and 1D trench arrays were

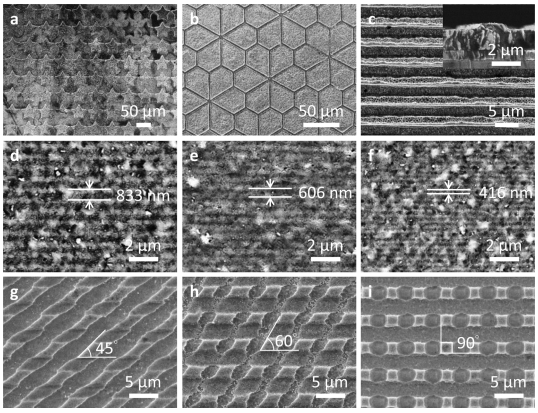

Figure 5. (a) CIGS microstar arrays; (b) CIGS microflower arrays; (c) CIGS micrograting; (d, e, f) MACE CIGS nanogratings with different periods of d, 833, e, 606 nm, and f, 416 nm; (g, h, i) cross-imprinting of CIGS microgratings with arrangement angles of g, 45°, h, 60°, and i, 90°.

demonstrated using corresponding structured agarose stamps by the MACE process as shown in parts a–c, respectively, of Figure 5 (see the Supporting Information). The high-fidelity arrays of microstructures indicate that agarose stamps can precisely transfer the desired patterns from the silicon master stamps on the CIGS films. Furthermore, submicron feature sizes from 833 to 416 nm can be obtained as shown in Figure 5d–f with an etching depth of ~200 nm. To make the best use of our MACE process, we performed the cross-imprinting process to get microstructure arrays aligned at varying angles including 45°, 60°, and 90° as shown in Figure 5g–i with the same agarose stamps. A detailed cross-imprinting process is described in Figure S5 (Supporting Information).

Furthermore, the MACE process can be applied to form CIGS MDAs and MHAs on CIGS thin films prepared by quaternary sputtering of Cu-poor and Cu-rich CIGS targets and electrodeposition followed by postselenization. As can be seen in Figure S6 (Supporting Information), CIGS MDAs or MHAs could be uniformly formed on the CIGS thin films regardless of the CIGS growth conditions. However, it should be noted that the surface roughness of pristine CIGS substrate may affect the final structures. A smooth surface of the CIGS thin film is desirable for the formation of micro- or nanostructures by the MACE process, while a rough surface of CIGS substrate after postselenization might result in indiscernible micro- or nanostructures.

The nanostructure on the absorber layer is an effective geometry for antireflection purposes, which have been demonstrated to enhance absorption ability with smooth transition of refractive index from the top nanostructure to the bottom film. However, the absorption behavior of the nanostructure could be significantly decreased after completion of the device fabrication process, restricting enhancement of the device performance.[32] However, this phenomenon can be overcome in our CIGS microstructures, owing

to unchanged microstructures after the device fabrication process. To elucidate the benefits of the CIGS microstructure arrays, we fabricate CIGS MDAs and MHAs solar cells with a conventional device fabrication process as described in the Experimental Section. Furthermore, a finite difference frequency domain (FDFD) algorithm was used to simulate distribution of electromagnetic fields in the four kinds of device configurations, including pristine CIGS thin films (pristine), CIGS thin films after the MACE process without patterns (without patterns), CIGS MDAs, and CIGS MHAs devices with detailed device configurations and tabulated optical constants of each layer as shown in Figure S7 (Supporting Information). As can be seen in Figure 6a, for the pristine sample, the incident wave would interfere with the reflected waves, resulting in obvious Fabry–Perot standing-wave resonance in wavelength ranges between 800 and 1000 nm, and the stronger Fabry–Perot standing-wave resonance can be found for the CIGS substrates without patterns due to the much thinner CIGS thin film. Remarkably, the CIGS MDAs and MHAs cell devices show the lower reflectance in the wavelength ranges between 800 and 1000 nm. The measured reflectance results are in good agreement with the simulated results. To better shed light on understanding the antireflection property, we selected the electric field intensity distribution at 875 nm for devices without patterns, MDAs, and MHAs configurations as shown in the left upper insets in parts b–d, respectively, of Figure 6. From the field distribution of device without patterns, the strong field intensity above the device structure can be found, which is ascribed to the refractive index differences between air and ITO and CIGS (left upper insets in Figure 6b). In contrast, the field intensity above the device structure can be significantly destroyed near the edge of the microstructures, and part of the field can be penetrated into the CIGS absorber and thus guided to longer optical path length, thereby reducing the intensity of Fabry–Perot resonance, especially for the CIGS MDAs (left upper insets in Figure 6c,d). As for the absorption distribution of devices without patterns shown in the right upper insets in Figure 6b, the absorption near the wavelength at 800 nm is ascribed to the region beneath the CdS/CIGS interface, but higher field distribution within ITO, ZnO, and CdS would not result in obvious absorption enhancement. The absorption enhancement of CIGS MDAs and MHAs can be ascribed to the guided waves penetrating through the edge of the CIGS microstructures and the window layers above (right upper insets in Figure 6c,d). To further verify the absorption enhancement contributing to the carrier generation, the generation rate and the current density (J) distribution were simulated as shown in the middle and lower insets in parts b–d, respectively, of Figure 6. Obviously, the enhanced generation rate can be achieved in the region whose the absorption is

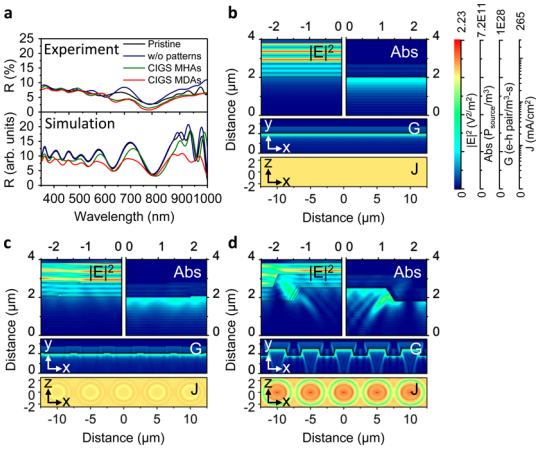

Figure 6. (a) Measured and FDTD-simulated reflectance of each devices. (b, c, d) FDTD simulated spatial distribution of the square of electric field intensity ($|E|^2$), absorption (Abs) at the wavelength of 875 nm, carrier generation rate (G), and photocurrent density (J) of (b) without patterns, (c) CIGS MDAs, and (d) CIGS MHAs devices.

enhanced by the guided field for CIGS MHAs and MDAs device, especially for CIGS MDAs device (middle insets in Figure 6b–d). In addition, the J distribution also shows locally enhanced photocurrents for CIGS MDAs and MHAs, with which the integrated J value of the CIGS with patterns, CIGS MHAs, and CIGS MDAs devices are 44.45, 45.33, and 47.57 mA/cm^2, respectively (lower insets in Figure 6b–d). In summary, the CIGS microstructures can serve as effective diffractors that diffract and guide the incident light into longer optical path and generate more electron–hole pairs.

To confirm our simulation results, the J–V characteristics under 1.5 G illumination solar light for pristine CIGS film, CIGS without patterns, CIGS MHAs, and MDAs devices are shown in Figure 7a, and the corresponding open-circuit potential (V_{OC}), short-circuit current (J_{SC}), fill factor (FF), and cell efficiency (η) for pristine CIGS, CIGS without patterns, CIGS MHAs, and CIGS MDAs are listed in Table 3. Note that the low leakage current can be confirmed from dark J–V curves for all devices as shown in Figure S8 (Supporting Information), indicating that the quality of the CIGS substrates was not deteriorated after the MACE processes. As a result, the V_{OC}, J_{SC}, and FF of 603 mV, 23.84 mA/cm^2, and 0.7 with the η of ~10.11% for the pristine CIGS device were measured while the reflectance increased owing to the reduction of the absorber thickness from ~2.5 to ~2.1 μm and the smoother surface of the CIGS device without patterns, leading to reduction of J_{SC} and, therefore, degradation of the η from 10.11 to 9.56%. In contrast, as for the device of CIGS MHAs, the enhanced J_{SC} from 23.64 to 25.73 mA/cm^2 with the enhanced η from 9.56 to 10.45% can be achieved. The highest enhanced η with 17.36% of the device of CIGS MDAs, compared with the CIGS without patterns device, with enhanced J_{SC}, FF, and η of 25.73 mA/cm^2, 0.72, and 11.22% can be

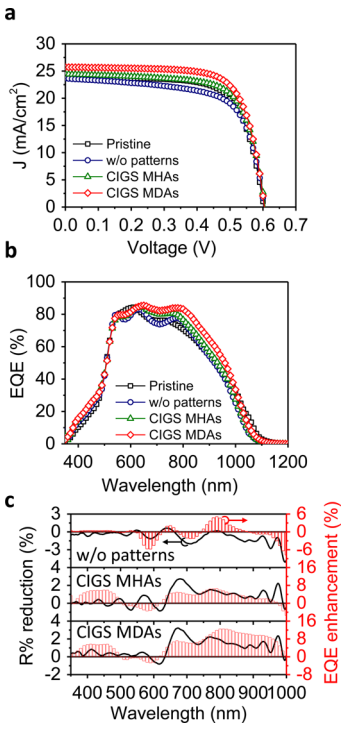

Figure 7. (a) Light *J*–*V* characteristics and (b) EQE measurements of devices of pristine, CIGS wigthout patterns, CIGS MHAs, and CIGS MDAs. (c) EQE enhancement and *R*% reduction *versus* wavelengths.

TABLE 3. Summary of the Photovoltaic Parameters

	V_{OC} (mV)	J_{SC} (mA/cm^2)	FF	efficiency (%)
pristine	603	23.84	0.70	10.11
without patterns	604	23.64	0.67	9.56
CIGS MHAs	607	24.47	0.70	10.45
CIGS MDAs	604	25.73	0.72	11.22

achieved, respectively, even if the thickness of the CIGS absorber was further decreased to ~1.9 μm. More device measurements are shown Figure S9a–d and Table S2 in the Supporting Information. Unlike most of the silicon-based nanostructure solar cells,[10,33] no obvious decrease in V_{OC} and FF was found, which should be attributed to the possible reason that the MACE process can increase the pattern height while reducing the roughness simultaneously. Therefore, the V_{OC} reduction would be the acceptable deviation (see the Supporting Information). Another reason should be the fact that most CdS/CuInGaSe$_2$ devices are dominated by bulk recombination instead of interface recombination due to the formation of buried homojunction caused by Cu-poor ordered defect compounds[34,35] and the close lattice-matching between the CIGS/CdS interface.[36] Moreover, Jehl *et al.* have also demonstrated that V_{OC} and FF of CIGS solar cells are independent of the surface roughness (from 230 to 90 nm) by similar bromine etching.[37]

The measured external quantum efficiency (EQE) of each device was measured as shown in Figure 7b, and

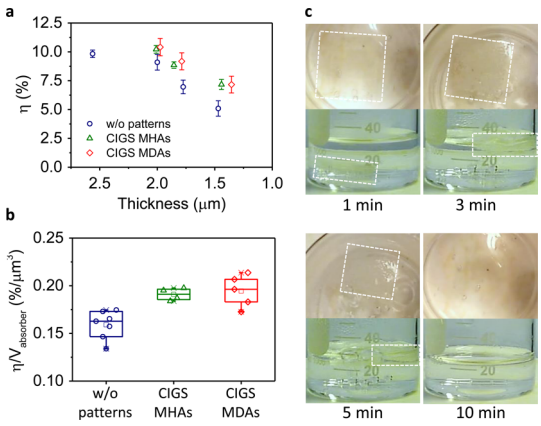

Figure 8. (a) Statistical efficiency (η) plotted against CIGS absorber thicknesses. (b) Efficiency per unit absorber volume of without patterns, CIGS MDAs, and CIGS MHAs devices. (c) Time-lapse video image sequences of dissolving an used agarose stamp observed from top and side view. The white dashed line boxes indicate the agarose stamp.

the reflectance reduction and the EQE enhancement rates as the function of the solar light wavelengths are plotted in Figure 7c. Note that the blue responses from the EQE from CIGS MDAs and MHAs devices are attributed to the variation thickness of the CdS layer due to the possible existence of the Se residual on the surface, resulting in thinner CdS layer.[38] Obviously, the enhanced light absorption with solar light wavelengths from 600 to 900 nm for CIGS MHAs and CIGS MDAs can be confirmed from EQE enhancements, which are in good agreement with the plot of the reflectance reduction rate.

Furthermore, the requirements for cost-effective photovoltaic application mainly focus on how to significantly reduce material usage while retaining the device efficiency. To address this issue, our MACE process enables the comparison of cell efficiencies with the same growth conditions but different thicknesses of CIGS without patterns, CIGS MHAs, and CIGS MDAs devices from 2 to 1.5 μm as shown in Figure 8a. Obviously, the efficiency of CIGS without patterns devices decrease monotonically with the absorber thickness reduction. In contrast, the CIGS MHAs and CIGS MDAs shows higher efficiency than that of their planar counterpart. Higher devices efficiency of either CIGS microstructures can be achieved at thicknesses of about 2 μm due to higher J_{SC} as shown in Table 3. However, the efficiency of devices either with or without microstructures decreases with the absorber thickness, which should be ascribed to the rear surface recombination. Furthermore, to confirm the maximal solar absorption in an absorber material with a given volume, the average efficiency per unit absorber volume is an important and requisite parameter to evaluate the usage of the materials.[10,31,32] The corresponding efficiencies per unit absorber volume ($\eta/V_{absorber}$) in a 5 μm × 5 μm unit cell for CIGS w/o patterns, CIGS MHAs, and CIGS MDAs devices were

compared as shown in Figure 8b. Interestingly, $\eta/V_{absorber}$ of ~0.159%/μm^3 for the CIGS w/o patterns device was found while the $\eta/V_{absorber}$ increases into ~0.191%/μm^3 and ~0.194%/μm^3 for the CIGS MHAs and CIGS MDAs devices, respectively, confirming the MACE process the cost-effective mothology.

Environmentally degradable polymers are reckoned as the most promising emission-free and eco-friendly materials since they, compared with other nondegradable solid wastes, can reduce long-term wastes disposal or storage issues and pose less harm to the disposal environment once the useful lifetime is reached. For example, high-resolution agarose can usually be reused for several time by the simple remelting process in the application of electrophoretic separation which is the routine method for resolving DNA.[39] To demonstrate the recycling of the agarose stamp, the used agarose stamp was soaked in the aqueous methanol solution for 24 h to elute most of the etchant and reaction products. Subsequently, the agarose stamp was placed in the boiling DI water with occasional swirling for the remelting process owing to the melting temperature of 90−95 °C of the agarose as shown in Figure 8c (see the video in the Supporting Information). The results indicate that the agarose stamp is hydrolytically degradable in the boiling DI water within 10 min. Our further objective is to reduce or eliminate the etchant in the gel matrix that are hazardous to human health or the environment, which is an important prerequisite for our integral pursuit of totally eco-friendly process.

CONCLUSION

We have demonstrated a bromine−methanol-based MACE process that enables the expeditious generation of large-area CIGS micro- or nanostructures with utmost ease. During the MACE process, the residual etchant inside the MPAs of agarose plays a pivotal role. By controlling the spreading of the residual etchant, either positive or negative relief micropattern arrays with a same agarose stamp can be achieved. The formation mechanism of micropatterns is attributed to the etch rate difference between the contact etching and the direct etching by the etchant inside and outside of the agarose matrix, respectively. From the surface chemical and structural properties investigated by XPS and Raman spectra, the Se-rich phase layer formed on the surface of CIGS substrate after 6 min MACE process would be oxidized and dissolved after longer MACE duration. To elucidate the advantages of our MACE process, we integrated the CIGS MDAs and MHAs into standard CIGS solar cell configurations. The absorption optical path lengthening due to the microdome arrays on the CIGS substrates can result in 17.36% enhancement in efficiency compared with that of its planar counterparts. It is anticipated that the technology demonstrated here could further improve the performance by structural optimization of CIGS microarrays devices and improving the uniformity of MACE process and could be extended to other thin film photovoltaic material systems, including CdTe and Cu_2ZnSnS_4, *etc.*, to enable high-efficiency textured thin film photovoltaics.

EXPERIMENTAL SECTION

Fabrication of Agarose Stamps. The stamps were made by pouring 8 wt % solution of agarose (LE-Agarose 1200, Taiwan Agar−Agar Industrial Co., Ltd.) in deionized water against a homemade silicon master stamp with a microrod arrays on its surface. The agarose solution was heated for 2 h at 95 °C in a vacuum oven. After degassing and eliminating bubbles, the hot agarose gel was taken out for cooling to room temperature. After gelation, the agarose gel were cut into 2 cm × 2 cm × 0.5 cm rectangular stamps.

FDTD Simulations. Simulation results were collected using finite difference time domain (FDTD) solver Lumerical solutions to study the reflectance, absorption, and generation properties of different types of CIGS structures. The detailed geometric design is shown in Figure S7 (Supporting Information) based on the SEM measurements. Three-dimensional simulations were conducted using a mesh size of 20 nm per grid point. Periodic boundary condition was imposed at the *xy* plane and *yz* plane to reduce the computational demand. The plane wavelight source was incident vertically above simulated solar cell devices with wavelengths from 200 to 1400 nm. A reflection monitor was placed above the light source, and a transmission monitor was placed beneath the Mo substrate. The simulations included both refractive indices (n) and extinction coefficients (k), accounting for absorption of each layers. For all layers, refractive indices are taken from references described in Figure S7 (Supporting Information). We calculated absorption with the equation $\mathrm{Abs}(\vec{r},\lambda) = -\frac{\pi c}{\lambda}|E(\vec{r},\lambda)|^2\mathscr{T}\{(\vec{r},\lambda)\}$ and calculated the generation rate profile with the equation $G(\vec{r},\lambda) = -\frac{|E(\vec{r},\lambda)|^2\mathscr{T}\{(\vec{r},\lambda)\}}{2\hbar}$ where $E(\vec{r},\lambda)$ is the electric field and $\mathscr{T}\{(\vec{r},\lambda)\}$ is the imaginary part of the permittivity. By integrating the absorption spectrum with a AM1.5 G solar spectrum, the integrated broadband absorption and ideal J_{SC} in CIGS with completely carrier collection can be obtained.

Device Fabrication and Measurements. Coevaporation growth of CIGS absorbers was deposited from elemental source effusion cells in a high-vacuum environment. The average film thickness, [Cu]/([Ga] + [In]), and [Ga]/([Ga] + [In]) of the CIGS layers are about ~2.56 μm, ~1.46 and ~0.82, respectively, as determined by scanning electron microscopy and energy dispersive spectroscopy. Devices are finished by chemical bath deposition (CBD) of a 50 nm thick buffer layer of CdS, sputtering of an i-ZnO/ITO window layer, and electron-beam evaporation of Al top electrodes. Single cells with an illuminated area of 0.125 cm^2 are defined by mechanical scribing. The device characteristics are measured under a solar simulator with standard-test conditions (A.M. 1.5 Global spectrum with 100 mW cm^{-2} intensity). $J-V$ and EQE characteristics were recorded using a Keithley 4200-SCS source meter and a QE-R3011 system (ENLI Technology Co., Ltd.), respectively. The EQE of the solar cells was measured with a lock-in amplifier. A chopped white light source (100 W, QTH lamp, 360 Hz) and a dual grating monochromator generated the probing beam. Certified monocrystalline Si and Ge cells from Fraunhofer ISE was used as the reference cell.

Characterization. Surface bonding states and chemical compositions of pristine and MACE CIGS substrates were examined by X-ray photoelectron spectroscopy (XPS, Perkin-Elmer Phi 1600 ESCA system, operated at beam current/accelerating voltage of 25 mA/15 kV, using a monochromatized Mg Kα X-ray source, respectively) with an energy resolution of ΔE = 0.05 eV,

which was calibrated by the Pt top electrode with a binding energy of $4f_{7/2}$ at 71 eV. Raman spectra were recorded by using laser micro-Raman spectroscopy: HORIBA Jobin-Yvon LabRAM HR800. A 514 nm laser was used as the excitation light source with an ×50 objective lens.

Conflict of Interest: The authors declare no competing financial interest.

Acknowledgment. The research is supported by Ministry of Science and Technology through Grant No. 101-2112-M-007-015-MY3, 101-2218-E-007-009-MY3, 103-2633-M-007-001, and the National Tsing Hua University through Grant No. 104N2022E1. Y.L.C. greatly appreciates the use of facility at CNMM, National Tsing Hua University through Grant No. 104N2744E1.

Supporting Information Available: SEM images of homemade silicon master stamp and agarose stamp agarose stamp; OM images of different regions and Raman spectra of CIGS MDAs; demonstration of various CIGS micro- and nanostructures, and cross-contact printing process by the MACE process; formation of CIGS MDAs and MHAs on various CIGS substrates; detailed FDTD simulations; dark *J*−*V* characteristic of pristine, CIGS without patterns, CIGS MHAs, and MDAs. This material is available free of charge *via* the Internet at http://pubs.acs.org

REFERENCES AND NOTES

1. Klaer, J.; Klenk, R.; Boden, A.; Neisser, A.; Kaufmann, C.; Scheer, R.; Schock, H. W. Damp Heat Stability of Chalcopyrite Mini-Modules: Evaluation of Specific Test Structures. *31st IEEE Photovoltaic Specialists Conference (PVSC)*, Lake Buena Vista, FL, **2005**; pp 336−339.
2. Hans-Werner, S.; Rommel, N. CIGS-Based Solar Cells for the Next Millennium. *Prog. Photovoltaics* **2000**, *8*, 151–160.
3. http://cleantechnica.com/2014/09/27/new-cigs-solar-cell-record-21-7-cigs-cell-conversion-efficiency-achieved-zsw/.
4. Feltrin, A.; Freundlich, A. Material Considerations for Terawatt Level Deployment of Photovoltaics. *Renew. Energy* **2008**, *33*, 180185.
5. Li, X. H.; Wei, E. I. S.; Wallace, C. H. C.; Dixon, D. S. F.; Xie, F. X. Efficient Inverted Polymer Solar Cells with Directly Patterned Active Layer and Silver Back Grating. *J. Phys. Chem. C* **2012**, *116*, 7200–7206.
6. Yang, K.-H.; Yang, J.-Y. The Analysis of Light Trapping and Internal Quantum Efficiency of a Solar Cell with Grating Structure. *Sol. Energy* **2011**, *85*, 419–431.
7. Wehrspohn, R.; Upping, J. 3D Photonic Crystals for Photon Management in Solar Cells. *J. Opt.* **2012**, *14*, 024003.
8. Halaoui, L. I.; Abrams, N. M.; Mallouk, T. E. Increasing the Conversion Efficiency of Dye-Sensitized TiO_2 Photoelectrochemical Cells by Coupling to Photonic Crystals. *J. Phys. Chem. B* **2005**, *109*, 6334–6342.
9. Atwater, H. A.; Polman, A. Plasmonics for Improved Photovoltaic Devices. *Nat. Mater.* **2010**, *9*, 205–213.
10. Jeong, S.; McGehee, M. D.; Cui, Y. All-Back-Contact Ultra-Thin Silicon Nanocone Solar Cells with 13.7% Power Conversion Efficiency. *Nat. Commun.* **2013**, *4*, 2950.
11. Wallentin, J.; Anttu, N.; Asoli, D.; Huffman, M.; Aberg, I.; Magnusson, M. H.; Siefer, G.; Fuss-Kailuweit, P.; Dimroth, F.; Witzigmann, B.; et al. InP Nanowire Array Solar Cells Achieving 13.8% Efficiency by Exceeding the Ray Optics Limit. *Science* **2013**, *339*, 1057–1060.
12. Huang, Y. F.; Chattopadhyay, S.; Jen, Y. J.; Peng, C. Y.; Liu, T. A.; Hsu, Y. K.; Pan, C. L.; Lo, H. C.; Hsu, C. H.; Chang, Y. H.; et al. Improved Broadband and Quasi-Omnidirectional Anti-Reflection Properties with Biomimetic Silicon Nanostructures. *Nat. Nanotechnol* **2007**, *2*, 770–4.
13. Liu, C. H.; Chen, C. H.; Chen, S. Y.; Yen, Y. T.; Kuo, W. C.; Liao, Y. K.; Juang, J. Y.; Kuo, H. C.; Lai, C. H.; Chen, L. J.; et al. Large Scale Single-Crystal Cu(In,Ga)Se_2 Nanotip Arrays for High Efficiency Solar Cell. *Nano Lett.* **2011**, *11*, 4443–4448.
14. Chang, Y.-A.; Li, Z.-Y.; Kuo, H.-C.; Lu, T.-C.; Yang, S.-F.; Lai, L.-W.; Lai, L.-H.; Wang, S.-C. Efficiency Improvement of Single-Junction InGaP Solar Cells Fabricated by a Novel Micro-Hole Array Surface Texture Process. *Semicond. Sci. Technol.* **2009**, *24*, 085007.
15. Yang, T.-C.; Lee, B.-S.; Yen, T.-J. Minimizing Reflection Losses from Metallic Electrodes and Enhancing Photovoltaic Performance Using the Si-Micrograting Solar Cell with Vertical Sidewall Electrodes. *Appl. Phys. Lett.* **2012**, *101*, 103902.
16. Kim, D. R.; Lee, C. H.; Rao, P. M.; Cho, I. S.; Zheng, X. Hybrid Si Microwire and Planar Solar Cells: Passivation and Characterization. *Nano Lett.* **2011**, *11*, 2704–2708.
17. Brendel, R.; Scholten, D. Modeling Light Trapping and Electronic Transport of Waffle-Shaped Crystalline Thin-Film Si Solar Cells. *Appl. Phys. A-Mater. Sci. Process.* **1999**, *69*, 201–213.
18. Deb, S. K. Frontiers in Photovoltaic Materials and Devices. *Curr. Opin. Solid State Mater. Sci.* **1998**, *3*, 51–59.
19. Jeong, S.; Garnett, E. C.; Wang, S.; Yu, Z.; Fan, S.; Brongersma, M. L.; McGehee, M. D.; Cui, Y. Hybrid Silicon Nanocone-Polymer Solar Cells. *Nano Lett.* **2012**, *12*, 2971–2976.
20. Jingbi, Y.; Xuanhua, L.; Feng-xian, X.; Wei, E. I. S.; Johnson, H. W. K.; Gang, L.; Wallace, C. H. C.; Yang, Y. Surface Plasmon and Scattering-Enhanced Low-Bandgap Polymer Solar Cell by a Metal Grating Back Electrode. *Adv. Energy Mater.* **2012**, *2*, 1203–1207.
21. Corsin, B.; Karin, S. d. m.; Jordi, E.; Franz-Josef, H.; Didier, D.; Peter, C.; Mathieu, B.; Grégory, B.; Céline, D.; Matthieu, D.; et al. Efficient Light Management Scheme for Thin Film Silicon Solar Cells *via* Transparent Random Nanostructures Fabricated by Nanoimprinting. *Appl. Phys. Lett.* **2010**, *96*, 213504.
22. Younan, X.; Dong, Q.; George, M. W. Microcontact Printing with a Cylindrical Rolling Stamp: A Practical Step toward Automatic Manufacturing of Patterns with Submicrometer-Sized Features. *Adv. Mater.* **1996**, *8*, 1015–1017.
23. Goetting, L.; Deng, T.; Whitesides, G. Microcontact Printing of Alkanephosphonic Acids on Aluminum: Pattern Transfer by Wet Chemical Etching. *Langmuir* **1999**, *15*, 1182–1191.
24. Grzybowski, B. A.; Bishop, K. J. M.; Campbell, C. J.; Fialkowski, M.; Smoukov, S. K. Micro- and Nanotechnology *via* Reaction−Diffusion. *Soft Matter* **2005**, *1*, 114.
25. Klajn, R.; Fialkowski, M.; Bensemann, I. T.; Bitner, A.; Campbell, C. J.; Bishop, K.; Smoukov, S.; Grzybowski, B. A. Multicolour Micropatterning of Thin Films of Dry Gels. *Nat. Mater.* **2004**, *3*, 729–35.
26. Crank, J.*The Mathematics of Diffusion*; Clarendon Press: Oxford, 1975.
27. Wagner, C.; Muilenberg, G. *Handbook of X-ray Photoelectron Spectroscopy*; Perkin-Elmer: Eden Prairie, 1979.
28. Seah, M. P.; Briggs, D. *Practical Surface Analysis: Auger and X-Ray Photoelectron Spectroscopy*; John Wiley & Sons: New York, 1993; Vol. 1.
29. Canava, B.; Guillemoles, J. F.; Vigneron, J.; Lincot, D.; Etcheberry, A. Chemical Elaboration of Well Defined Cu(In,Ga)Se_2 Surfaces after Aqueous Oxidation Etching. *J. Phys. Chem. Solids* **2003**, *64*, 1791–1796.
30. Bandyopadhyay, T.; Chakraborty, S.; Chaudhuri, S. Effect of Surface Treatment on the Photoanodic Behaviour of Thin Film n-CdSe. *Phys. Status Solidi A* **1988**, *108*, K119–K123.
31. Yannopoulos, S. N.; Andrikopoulos, K. S. Raman Scattering Study on Structural and Dynamical Features of Noncrystalline Selenium. *J. Chem. Phys.* **2004**, *121*, 4747–58.
32. Liao, Y.-K.; Wang, Y.-C.; Yen, Y.-T.; Chen, C.-H.; Hsieh, D.-H.; Chen, S.-C.; Lee, C.-Y.; Lai, C.-C.; Kuo, W.-C.; Juang, J.-Y.; et al. Non-Antireflective Scheme for Efficiency Enhancement of Cu(In,Ga)Se_2 Nanotip Array Solar Cells. *ACS Nano* **2013**, *7*, 7318–7329.
33. Shen, X.; Sun, B.; Liu, D.; Lee, S.-T. Hybrid Heterojunction Solar Cell Based on Organic−Inorganic Silicon Nanowire Array Architecture. *J. Am. Chem. Soc.* **2011**, *133*, 19408–19415.
34. Klenk, R. Characterisation and Modelling of Chalcopyrite Solar Cells. *Thin Solid Films* **2001**, *387*, 135–140.
35. Jiang, C.-S.; Hasoon, F.; Moutinho, H.; Al-Thani, H.; Romero, M.; Al-Jassim, M. Direct Evidence of a Buried

Homojunction in Cu(In, Ga)Se_2 Solar Cells. *Appl. Phys. Lett.* **2003**, *82*, 127–129.
36. Abou-Ras, D.; Kostorz, G.; Romeo, A.; Rudmann, D.; Tiwari, A. N. Structural and Chemical Investigations of CBD- and PVD-CdS Buffer Layers and Interfaces in Cu(In,Ga)Se_2-Based Thin Film Solar Cells. *Thin Solid Films* **2005**, *480–481*, 118–123.
37. Jehl, Z.; Bouttemy, M.; Lincot, D.; Guillemoles, J. F.; Gerard, I.; Etcheberry, A.; Voorwinden, G.; Powalla, M.; Naghavi, N. Insights on the Influence of Surface Roughness on Photovoltaic Properties of State of the Art Copper Indium Gallium Diselenide Thin Films Solar Cells. *J. Appl. Phys.* **2012**, *111*, 114509.
38. Kay, O.; Uwe, R.; Quang, N.; Hans Werner, S.; Jurgen, H. W. Role of the CdS Buffer Layer as an Active Optical Element in Cu(In,Ga)Se_2 Thin-Film Solar Cells. *Prog. Photovoltaics* **2002**, *10*, 457–463.
39. Seng, T. Y.; Singh, R.; Faridah, Q. Z.; Tan, S. G.; Alwee, S. S. Recycling of Superfine Resolution Agarose Gel. *Genet. Mol. Res.* **2013**, *12*, 23602367.